

A Molecular Engineering Approach to Conformationally Regulated Conductance Dualism in a Molecular Junction

Moritz Nau, William Bro-Jørgensen, Michael Linseis, Michael Bodensteiner, Rainer F. Winter,* and Gemma C. Solomon*

Abstract: One key aspect for the development of functional molecular electronic devices is the ability to precisely tune and reversibly switch the conductance of individual molecules in electrode-molecule-electrode junctions in response to external stimuli. In this work, we present a new approach to access molecular switches by deliberately controlling the flexibility in the molecular backbone. We here describe two new conductance switches based on bis(triarylaminines) that rely on the reversible toggling between two conformers, each associated with vastly different conductances. By molecular design, we were able to realize an *on/off* ratio $G_{\text{high}}/G_{\text{low}}$ of $\sim 10^3$, which is one of the largest values reported to date. Flicker noise analysis and molecular transport calculations indicate that *on/off* switching relies on a change of the conduction pathway and vast differences in molecule-electrode coupling. We thereby provide a new scaffold for further development of molecular conductance switches that are both efficient and easily refined.

Introduction

One major challenge in the realm of molecular electronics is to create miniaturized functional devices that are capable of mimicking the components of traditional electronic circuits.^[1] As the function of such devices is encoded in their molecular architecture, the rich toolbox of synthetic chemistry offers nearly unlimited possibilities to purposefully design molecules and instill specific properties into them. One example are molecule-based switches,^[2] whose conductance can be reversibly altered in response to an external stimulus, such as a change of temperature,^[3] pH,^[4] or the redox state (i.e. by an applied potential),^[5] by electric fields,^[6] by light-induced changes of the molecular backbone,^[7] or by mechanical stress.^[7b,8] The Figure-of-merit of such switches is the *on/off* ratio, which measures the differences in conductance between the more and the less conductive states. Computational studies suggest that *on/off* ratios of up to the order of 10^4 are feasible.^[8c] The performances of literature-known molecular switches fall however considerably short of this promise, with *on/off* ratios of the order of 5–500.^[8b,c,f,9]

Among the different methods to stimulate conductance switching, mechanical triggering is particularly attractive, because it is easy to implement and obviates the use of exogenous chemical effectors or input, such as electrical fields, which may also induce isomerization, e.g. in allenes.^[6] Single-molecule conductance switches translate conformational changes into different preferred conductance pathways as these molecules are forced to adapt to a changing nanojunction structure on stretching or compression. Previously reported single-molecule conductance switches include imidazolyl-terminated alkanes,^[10] ferrocene derivatives,^[8a,c] diketones,^[8f] 4,4'-bipyridine,^[8g] and coordination compounds.^[11]

We here employ the thiomethyl-(SMe–) substituted bis(triarylaminines) (BTAAAs) **A_{Stilb}** and **A_{Biph}** with either two or three molecular gears encoded within their molecular backbones (see the right panel of Figure 1). Rotation around chemical bonds causes large-amplitude alterations of the spatial separations between their SMe anchor groups and of the molecule-electrode coupling, which in turn leads to vastly different molecular conductances for the different conformers.

Specifically, we were able to attenuate, by molecular design, the molecular conductance in the *off* state by one order of magnitude and to thereby increase the *on/off* ratio to $\sim 10^3$. Closely related, rigidified, cyclic molecules that lack

[*] M. Nau, Dr. M. Linseis, Prof. R. F. Winter
 Department of Chemistry
 University of Konstanz
 Universitätsstraße 10, 78464 Konstanz (Germany)
 E-mail: rainer.winter@uni-konstanz.de

W. Bro-Jørgensen, Prof. G. C. Solomon
 Nano-Science Center and Department of Chemistry
 University of Copenhagen
 Universitetsparken 5, 2100 København Ø (Denmark)
 E-mail: gsolomon@chem.ku.dk

Dr. M. Bodensteiner
 Faculty of Chemistry and Pharmacy
 University of Regensburg
 Universitätsstraße 31, 93053 Regensburg (Germany)

Prof. G. C. Solomon
 NNF Quantum Computing Programme, Niels Bohr Institute,
 University of Copenhagen, 2100 København Ø (Denmark)

© 2024 The Author(s). Angewandte Chemie International Edition published by Wiley-VCH GmbH. This is an open access article under the terms of the Creative Commons Attribution License, which permits use, distribution and reproduction in any medium, provided the original work is properly cited.

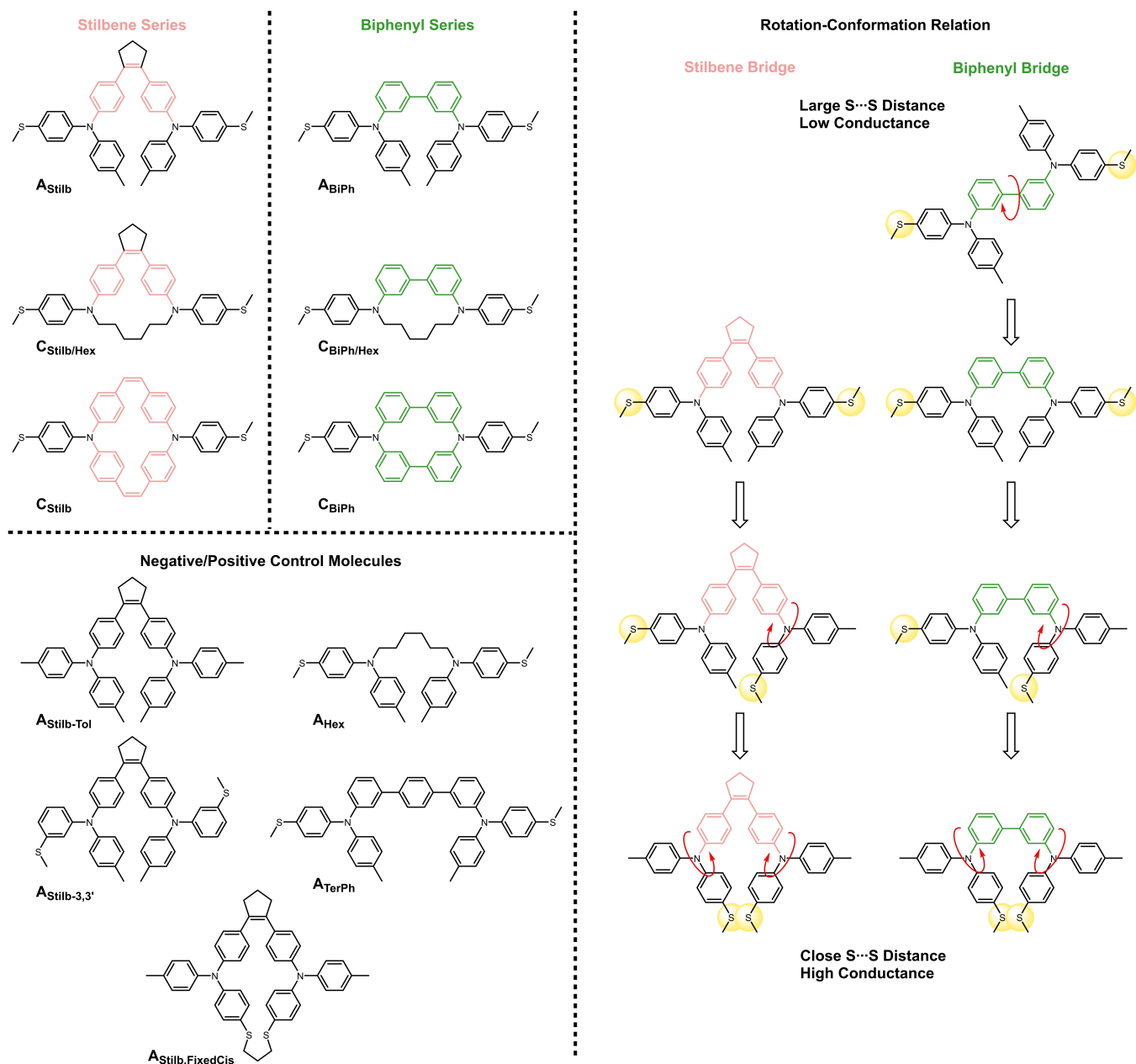


Figure 1. Chemical structures of the investigated linear and macrocyclic bis(triarylamines) (top left panel) and of various test molecules (bottom left panel). Different conformers of A_{Stilb} and A_{BiPh} as a result of different rotations are indicated by red, circular arrows (right panel).

this conformational degree of freedom or restrain A_{Stilb} to the *cisoid* conformation serve as negative or positive controls, but do not display conductance switching.

Results and Discussion

The two series of bis(triarylamines) devised for the present study are shown in Figure 1. The freely rotating NAr₂ moieties endow molecules A_{Stilb} and A_{BiPh} with two rotational axes each. Common to the members of the **Stilb** series is a *cis*-configured stilbenyl-type bridge, as imposed by the central cyclopentene unit. Congeners of the **BiPh** series

share a common 3,3'-biphenyl bridge, thereby offering an additional degree of conformational freedom through rotation around the central C–C bond. These molecular architectures thus allow for large variations of the S...S distances in response to an opening or closing of the Au–Au nanogap (see Figure 1). Rotations around the C–N bonds that connect the N(C₆H₄CH₃)(C₆H₄SMe) (NPh^{Me}Ph^{SMe}) endgroups to the linker is shut down in the cyclic analogs C, which precludes close approach of the S atoms. All compounds presented in this work were synthesized by standard C–N, and C–C cross-coupling protocols and characterized by NMR spectroscopy, mass spectrometry, elemental analysis, and, in the case of A_{Stilb}, C_{Stilb}/Hex, a

derivative of $\mathbf{C}_{\text{Stilb}}$, $\mathbf{A}_{\text{Stilb,FixedCis}}$, $\mathbf{A}_{\text{Stilb-Tol}}$, \mathbf{C}_{BiPh} , $\mathbf{C}_{\text{BiPh/Hex}}$, \mathbf{C}_{Hex} , as well as some intermediate products by X-ray diffraction experiments on single crystals.^[12] Pertinent information is provided in the Electronic Supporting Information (ESI[†]).

Molecular Conductance Measurements

The conductive properties of the BTAs of Figure 1 were investigated by the scanning tunneling microscopy break-junction (STM-BJ) technique according to established designs and protocols.^[11a,13] All STM-BJ experiments were conducted under ambient atmosphere and at room temperature. Further details of the used setup and the experimental procedure are provided in the ESI[†]. Figure 2 shows conductance histograms constructed from at least 5000 individual conductance versus displacement measurements of each member of the **Stilb** and **BiPh** series of Figure 1. And Table 1 summarizes the experimental and theoretical data from STM-BJ experiments and DFT based transport calculations, which will be discussed later. Within the **Stilb** series, acyclic $\mathbf{A}_{\text{Stilb}}$ is distinguished from its cyclic congeners $\mathbf{C}_{\text{Stilb}}$ and $\mathbf{C}_{\text{Stilb/Hex}}$ by its bimodal conductance distribution with two narrow, well-defined peaks at $9.2 \times 10^{-4} G_0$ and $1.5 \times 10^{-5} G_0$ (cf. panel A of Figure 2). G_0 denotes the quantum conductance, $G_0 = 2e^2/h$. The cyclic analogs $\mathbf{C}_{\text{Stilb}}$ and $\mathbf{C}_{\text{Stilb/Hex}}$ display only a single conductance peak at $5.2 \times 10^{-6} G_0$ ($\mathbf{C}_{\text{Stilb/Hex}}$) and $3.5 \times 10^{-5} G_0$ ($\mathbf{C}_{\text{Stilb}}$), respectively, as the most probable conductance values, which both resemble the low conductance (low- G) peak of $\mathbf{A}_{\text{Stilb}}$. Comparison of the associated 2D histograms and of individual conductance traces in panels B to D of Figure 2 reveal that the low- G features of all three BTAs are associated with uniform rupture lengths of ca. 0.9 nm. This translates into molecular lengths of ca. 1.4 nm when considering the snapback correction, which accounts for the structural reorganization and relaxation of the Au nanoelectrodes after rupture of a molecule-Au point contact.^[8j,14] The experimental maximum junction length is slightly shorter than the S...S distance of $\mathbf{C}_{\text{Stilb}}$ of 1.99 nm as determined by X-ray crystallography (values in brackets in Table 1). We thus infer that the low- G features belong to molecules in stretched conformations between the two gold leads with their SME anchor groups far apart (Figure 1, top right), but not with the maximum possible S...S distance, as regularly observed for long, flexible molecular wires.^[8c,f,11b,15] The high- G feature of $\mathbf{A}_{\text{Stilb}}$ however ends abruptly at ca. 0.3 nm (0.8 nm effective junction length), suggesting that it pertains to a compressed, *cisoid* conformer with a much closer approach of the SME anchor groups, which is also well reproduced by our DFT calculations showing an electrode-electrode distance of 0.84 nm in the high- G state (cf. Table 1 and the Computational Calculations chapter). As exemplified by the three representative, individual traces in the inset of panel B, only in a minority of traces the conductance directly decays into the low- G feature of $\mathbf{A}_{\text{Stilb}}$. Instead, the majority of traces of $\mathbf{A}_{\text{Stilb}}$ show the high- as well as the low- G features, so that both must originate from the same molecule. In all traces showing both features, the high- G feature precedes the low-

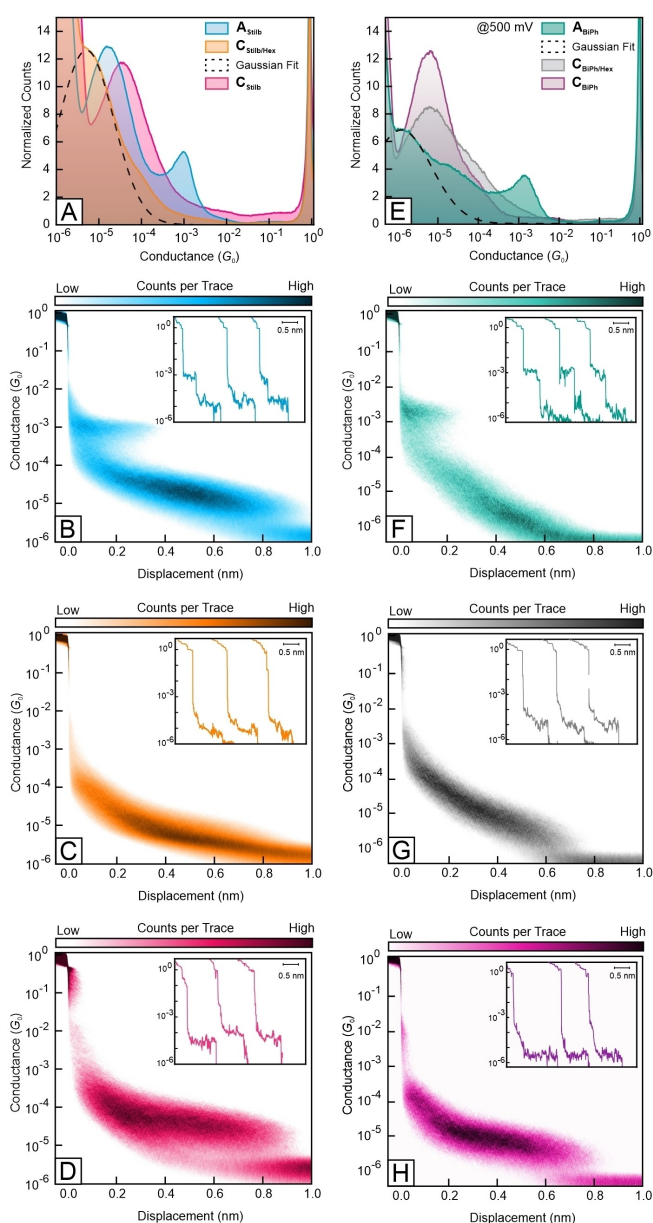


Figure 2. Logarithmically binned one-dimensional conductance histograms of the stilbenyl- and the 3,3'-biphenyl-bridged compounds $\mathbf{A}_{\text{Stilb}}$, $\mathbf{C}_{\text{Stilb}}$, and $\mathbf{C}_{\text{Stilb/Hex}}$ (A) and \mathbf{A}_{BiPh} , \mathbf{C}_{BiPh} , and $\mathbf{C}_{\text{BiPh/Hex}}$ (E) with their corresponding two-dimensional conductance vs. displacement histograms (1 mM solution of the analytes in 1,2,4-trichlorobenzene (TCB)) at $V_{\text{bias}} = 100$ mV (B: $\mathbf{A}_{\text{Stilb}}$, C: $\mathbf{C}_{\text{Stilb}}$, and D: $\mathbf{C}_{\text{Stilb/Hex}}$) or 500 mV (F: \mathbf{A}_{BiPh} , G: \mathbf{C}_{BiPh} , and H: $\mathbf{C}_{\text{BiPh/Hex}}$). All histograms were constructed from at least 5000 individual conductance vs. displacement measurements. Representative single traces in the inserts are shown with a lateral offset for better visibility.

G one. This indicates that frequently, at small gap extensions, molecules of $\mathbf{A}_{\text{Stilb}}$ are initially trapped in the high- G state, which then changes into the low- G state upon widening the Au nanojunction. $\mathbf{A}_{\text{Stilb}}$ thus constitutes a conductance switch which is based on the interconversion between *cisoid* and *transoid* conformers, associated with small and large S...S distances, resulting from rotations

Table 1: Compiled experimental and theoretical data from STM-BJ experiments and DFT based transport calculations of the cyclic and acyclic bis(triarylamines).

	Molecular Conductance		Junction Length (nm)		
	Experimental (G_0)	Calc. Transmission $T(E_F)$	Experimental	Corrected ^[a]	Calc. Electrode Displacement ^[b]
A_{Stilb}	$1.5 \times 10^{-5} 9.2 \times 10^{-4}$	$2.01 \times 10^{-5} 2.8 \times 10^{-4}$	0.90 0.30	1.40 0.80	1.98 [2.0052(5)] 0.84
C_{Stilb/Hex} ^[c]	5.2×10^{-6}	3.00×10^{-7}	0.90	1.40	1.90 [1.83848(14)]
C_{Stilb}	3.5×10^{-5}	1.62×10^{-5}	0.90	1.40	2.45 [1.98708(7)] ^[d]
A_{BiPh} ^[c]	$1.2 \times 10^{-6} 1.3 \times 10^{-3}$	$1.54 \times 10^{-8} 2.2 \times 10^{-3}$	0.80 0.25	1.30 0.75	2.17 0.91
C_{BiPh/Hex}	6.2×10^{-6}	1.70×10^{-7}	0.70	1.20	2.13 [1.7604(3)]
C_{BiPh}	6.1×10^{-6}	2.46×10^{-6}	0.80	1.30	2.12 [1.8811(2)]
A_{Stilb,FixedCis}	3.5×10^{-3}	—	0.30	0.80	[0.5027(2)]

[a] Applying an empirical snap-back correction of 0.5 nm; for further details note ref. [8j, 14a,b]. [b] Crystallographically determined S...S distances in brackets. [c] Experimental conductance values obtained by gaussian deconvolution of the one-dimensional conductance histogram. [d] Crystallographic data corresponds to a derivative with the same backbone structure. For further information see ESI[†].

around the N-Aryl bonds (Figure 1, right), and with an *on/off* ratio $G_{\text{high}}/G_{\text{low}}$ of ca. 60.

The absence of the high- G peak in the control molecules **C_{Stilb}** and **C_{Stilb/Hex}**, whose cyclic structures preclude *cisoid* structures and the close approach of the SMe anchor groups, confirms the proposed mechanism of conformational switching in **A_{Stilb}**. As a further test for this hypothesis, we devised and investigated **A_{Stilb,FixedCis}**, where a propyl tether clamps the aurophilic thio anchor groups together and confines them to a *cisoid* arrangement.

The most probable conductance value and associated feature lengths of **A_{Stilb,FixedCis}** indeed resemble the high- G feature of **A_{Stilb}** (see Figure S5 in the ESI[†]) closely, while lacking the low- G one. We however note that electron transmission in **A_{Stilb,FixedCis}** might as well propagate through the σ -system of the propyl linker, as related anchor group-terminated propanes show similar conductance values.^[13b,16]

The above results hence provide strong indications that the high- G state of **A_{Stilb}** primarily relies on the close spatial approach of the electrode-binding anchor groups, while the low- G state pertains to conductance across the molecular backbone. We therefore mused that replacing the rigid, π -conjugated *cis*-stilbenyl linker with a *meta,meta*-biphenylene motif with its inherent destructive quantum interference (DQI)^[17] is a viable way to increase the *on/off* ratio of our conformational switch. Such modification should diminish the electronic conductance of the low- G feature, yet without affecting that at high- G . To these ends, we devised acyclic **A_{BiPh}**, along with cyclic control molecules **C_{BiPh}** and **C_{BiPh/Hex}** (Figure 1).

Gratifyingly, **A_{BiPh}** exhibits a multimodal conductance distribution with a distinct high- G feature. Like for **A_{Stilb}**, the latter is insensitive towards mechanical stress and aligns almost horizontally with displacement. This leads to a narrow conductance distribution peaking at $1.2 \times 10^{-3} G_0$ in the 1D histogram (see panels E and F of Figure 2) until up to 0.25 nm (0.75 nm effective junction length), where it abruptly changes into the low- G state. As we had hoped, the low- G feature of **A_{BiPh}** is associated with distinctly smaller conductance values compared to **A_{Stilb}** and is now superimposed by the electrical background noise at low bias voltages (see also Figure S7 in the ESI[†]). However, we note that the low- G distribution of **A_{BiPh}** is notably broad and

also shows distinct counts in the range of 10^{-4} to $10^{-5} G_0$, which we attribute to other conformers in between the pure *cisoid* and *transoid* structures that will be traversed during a pulling experiment (see also Figure S22 and S23 in the ESI[†]). Increasing the bias voltage to 500 mV shifts the background to lower conductances and increases the molecular conductance, thereby exposing the low- G feature at $1.2 \times 10^{-6} G_0$. The conductance of the low- G feature is thus by more than one order of magnitude smaller than that of **A_{Stilb}**, which concomitantly increases the *on/off* ratio $G_{\text{high}}/G_{\text{low}}$ from ca. 60 in **A_{Stilb}** to $\sim 10^3$ in **A_{BiPh}**. This renders **A_{BiPh}** one of the best-performing molecular conductance switches reported in the literature.^[8b,c, f] Further increasing the bias voltage beyond 500 mV leads to a general broadening of the low- G feature with a more pronounced shoulder at the high- G end (cf. Figure S7). We muse that bias voltages > 500 mV generate small amounts of the oxidized forms, thereby causing the observed broadening of the low- G feature, as has been observed for other BTAAAs.^[5b]

As for **A_{Stilb}**, most individual traces recorded from **A_{BiPh}** show both features side by side, with the high- G plateau always preceding the low- G one. A peculiarity of **A_{BiPh}** is a distinct tailing of the low- G feature towards slightly higher conductance values, which endows the low- G peak with an asymmetric shape. This observation is also reflected in variations of the associated conductance values by about one order of magnitude for individual traces of **A_{BiPh}** (cf. inset in panel F of Figure 2). Tailing is attenuated in the rigidified macrocyclic congeners of **A_{BiPh}**, which show better defined, sharper conductance distributions maximizing at $6.2 \times 10^{-6} G_0$ (**C_{BiPh/Hex}**), and $6.1 \times 10^{-6} G_0$ (**C_{BiPh}**), respectively. Selected individual conductance vs. displacement measurements are provided as insets in panels G and H of Figure 2. In agreement with previous literature, we attribute the broadening of the conductance distributions for the members of the **BiPh** series to increased conformational freedom offered by the additional rotational axis within the molecular backbone and the sensitivity of molecular conductance to torsion around the biphenyl linkage.^[5b,18] This also explains the steeper slope and more distinct tailing of the 2D histograms of **C_{Stilb/Hex}** and **C_{BiPh/Hex}** as compared to **C_{Stilb}** and **C_{BiPh}**, where one of the arylene linkers is replaced by a more flexible hexyl chain. In all cases, the maximum feature

lengths for the low- G state range from 1.3 to 1.4 nm after snapback correction, which compares rather favorably with the maximum length of ca. 1.97 nm for fully erected molecules.

We also note that introducing a second π -conjugated conduction pathway in $\mathbf{C}_{\text{Stilb}}$ increases molecular conductance at large tip displacement (i.e. for the low- G feature) by a factor of 2.3 with respect to $\mathbf{A}_{\text{Stilb}}$, and by a factor of 6.7 with respect to $\mathbf{C}_{\text{Stilb/Hex}}$. This is possibly due to constructive conductance quantum interference (CQI) between two parallel conduction paths.^[19] In contrast, replacement of the hexyl for the biphenyl linker leaves the conductance unaltered in the congeners of the **BiPh** series.

To test the limits of our switching concept, we also investigated the hexyl-bridged bis(triarylamines) \mathbf{C}_{Hex} , \mathbf{A}_{Hex} (Figure 1 and ESI[†]), where the conductance of the *off* state relies on pure σ -transmission, as well as *cis*-stilbenyl-bridged $\mathbf{A}_{\text{Stilb-3,3'}}$ (Figure 1), where the SMe anchor groups at the outer phenyl rings are in *meta* positions. Unfortunately, these molecules did not exhibit defined conductance peaks. Similarly, the introduction of a terphenylene bridge in $\mathbf{A}_{\text{TerPh}}$ (Figure 1) subdued the low- G feature below the electrical noise floor, but also increased the S...S distance in the conformation with closer spacing of the anchor groups, which rendered the high- G state inaccessible (for further details see Figure S4 and S10–S12 in the ESI[†]).

Furthermore, we did not observe any molecular conductance signatures for $\mathbf{A}_{\text{Stilb-Tol}}$, which lacks the anchoring thiomethyl functionalities (for further details see Figure S2 in the ESI[†]). This is in line with earlier findings, which indicated that tertiary triarylamines (TAAs) without aurophilic functional groups are incapable of forming stable electrode-molecule-electrode junctions.^[5b]

Reversible Conductance Switching by Varying Tip Displacement

We next sought to further confirm our hypothesis of tip displacement-, conformationally-imposed conductance switching between the high- and low- G states. To these ends, we performed additional experiments, where the tip displacement was alternately changed by mechanically compressing and expanding the junction, which is a well-established test for mechanosensitive junctions.^[8b,f,j,20] We chose $\mathbf{A}_{\text{Stilb}}$ as test system, because the conductance distributions of both, the high- and the low- G features, are narrow, well-defined, and clearly distinguished from the electrical background noise level, even at low bias voltages. The applied push-pull sequence started with a linear pull to a nanogap extension, where, according to the previous results, a stable Au-molecule-Au junction is likely to form. After holding this particular excursion for 50 ms, the nanogap was repeatedly expanded and compressed by 0.8 nm. Every manipulation of the junction was followed by a holding time of 50 ms, during which the junction length was kept constant.

The applied non-linear displacement sequence is depicted in panel A of Figure 3. Panel B of Figure 3 shows that stepwise modulation of the junction expansion reliably

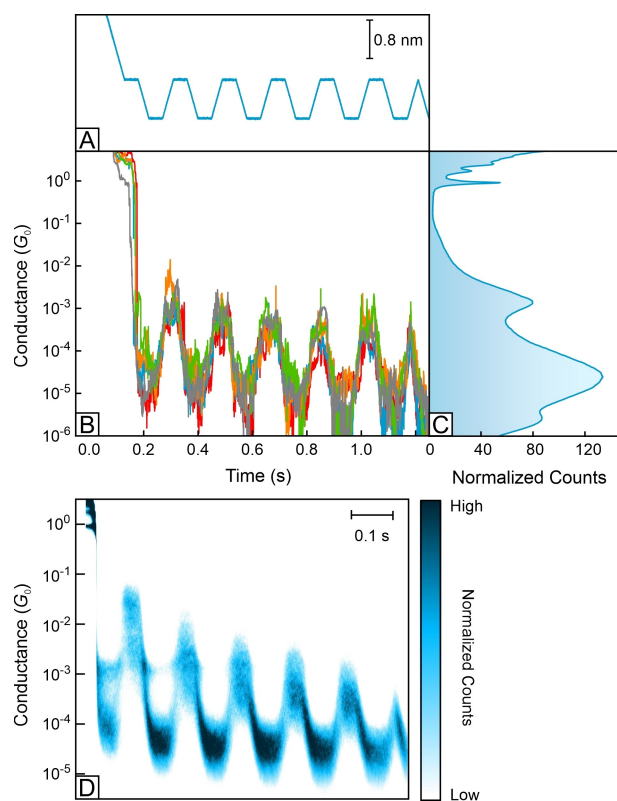


Figure 3. A: Non-linear displacements sequence applied for the mechanically controlled conductance switching experiments of $\mathbf{A}_{\text{Stilb}}$ with a switching amplitude of 0.8 nm. B: Selected individual conductance vs. time traces showing a switching of the conductance value following the applied displacement sequence, measured at 100 mV bias voltage. C: Conductance histogram constructed from 10000 individual switching experiments without data selection. D: Logarithmically binned two-dimensional conductance histogram as a function of tip displacement obtained from 10000 individual push-pull measurements of $\mathbf{A}_{\text{Stilb}}$ (1 mM in 1,2,4-TCB) without data selection applying a bias voltage of 100 mV.

switched the junction between the high- and low- G state of $\mathbf{A}_{\text{Stilb}}$ over several cycles of approaching or retracting the tip, once a molecule was successfully trapped within the junction. The one-dimensional conductance histogram constructed from 10000 individual push-pull experiments in panel C of Figure 3 shows the same high- and low- G features as were observed the 1D histogram with linear piezo modulation (cf. panel A of Figure 2). Panel D of Figure 3 compiles the individual push-pull experiments into a two-dimensional histogram, which consistently shows the mechanically induced stepwise modulation of the molecular conductance. However, there is a gradual decrease in the conductance in these switching experiments observed, which is frequently encountered in the literature albeit often less pronounced,^[8b,j,k] and can depend on several factors such as mechanical uncertainties of the used setup as well as problems in reliably hitting one of the two different states in later cycles of the switching experiment. In our case, the high- G state appears to be more affected than the low- G state, and we attribute this conductance decay to a

combination of setup-induced mechanical error and the loss of the idealized high- G configuration in later cycles caused by the highly flexible molecular backbone. Taken together, we measure the conductance of increasingly mixed configurations in later cycles (see also Figure S23 and S24 for the calculated transmissions of the mixed conformations). We also explored the influence of tip displacement rate by varying the push-pull rate from $10 \text{ nm} \cdot \text{s}^{-1}$ to $40 \text{ nm} \cdot \text{s}^{-1}$ and found no noticeable impact of higher rates on the switching behavior (see Figure S17 in the ESI[†]). At slower rates, the decay of the high- G state increases, which is probably the result from the larger impact of setup-induced mechanical errors that become more manifest on a longer timescale. When subjected to the same experiment, **A**_{BiPh} shows similar switching properties (see Figure S15 and S16 in the ESI[†]). However, the increased flexibility of **A**_{BiPh} ultimately blurs the conductance distributions for the two conductive states. In summary, we were able to mechanically and reversibly switch between the two conductive states of **A**_{Stilb} and **A**_{BiPh} over several cycles by periodically altering the tip displacement. This certifies that conductance switching is intimately tied to conformational changes of the molecule trapped within the junction.

Computational Studies

The large differences in conductance values between the compressed, high- G , and stretched, low- G , conformations of acyclic **A**_{Stilb} and **A**_{BiPh} suggested that the conformation change comes with differing transmission pathways. We therefore calculated the Landauer transmission for all members of the **Stilb** and **BiPh** series (a detailed description of the theoretical procedure is provided in the ESI[†]). The transmission paths were identified by calculating the current densities through the molecule using wideband approximated electrodes represented by dihydrogen.^[21] For visualizing the conductance pathway, current densities are represented by arrows, where each arrow is color-coded by its normalized z -component. Arrow sizes are normalized to the one with the largest magnitude in each respective molecule, so that they can be compared in only a qualitative sense.

Conformational change has indeed a profound impact on the preferred transmission pathway, as shown in the inserts of panels A and B of Figure 4. Thus, for the *transoid*, low- G conformer, the transmission path mainly passes through the π -system. In the *cisoid* structure associated with the high- G state, the transmission pathway takes a shortcut across the spatially close thiomethyl linkers.

Gratifyingly, the computed values for the low- and high- G conformers of **A**_{Stilb} at the Fermi level differ by one order of magnitude (cf. panel C of Figure 4 and Table 1). Differences are even larger for **A**_{BiPh} (ca. five orders of magnitude), where the shortcut through the SMe functionalities in the high- G conformer avoids the DQI feature inherent to the *meta,meta*-biphenyl motif. The latter becomes manifest through dips in the transmission plots. We also note much stronger interactions between the phenyl

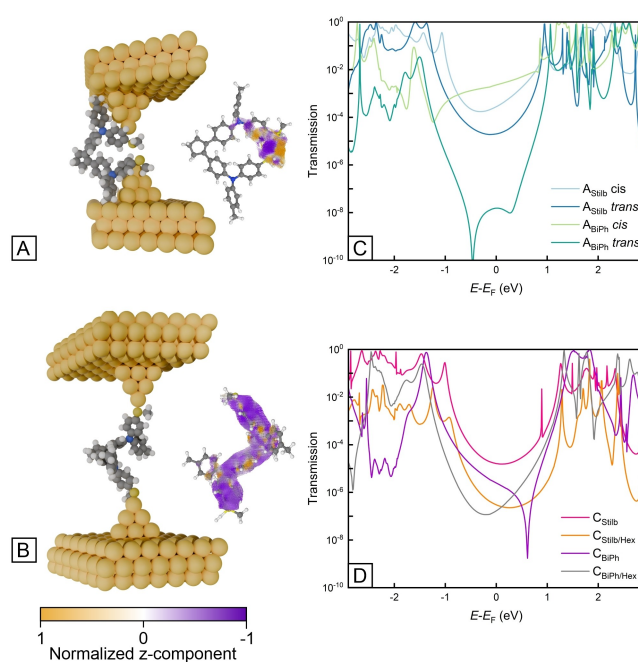


Figure 4. A: DFT optimized structure of **A**_{Stilb} with short S...S distance used for the transport calculation. B: DFT optimized structure of **A**_{Stilb} with long S...S distance used for the transport calculation. Current vector fields of the *cisoid* (A) and *transoid* (B) conformation of **A**_{Stilb} calculated on a high-density grid and colored by the z -component are provided as insets. C: $T(E)$ curves for acyclic molecules **A**_{Stilb} and **A**_{BiPh} in their relaxed (*transoid*) and compressed (*cisoid*) junction conformations. D: $T(E)$ curves for cyclic molecules **C**_{Stilb}, **C**_{Stilb/Hex}, **C**_{BiPh}, and **C**_{BiPh/Hex}.

moieties of the TAA fragments and the gold nanoelectrodes in the *cisoid* structure. The concomitant increase in molecule-electrode coupling is expected to also have a beneficial effect on conductance.

Our transmission calculations thus provide an excellent match with our experimental findings, although DFT-based methods tend to overestimate the conductance values.^[22] The latter also pertains to the cyclic analogs, whose transmission curves are shown in panel D of Figure 4. In particular, they accurately reproduce the higher conductance of **C**_{Stilb} versus **C**_{Stilb/Hex}, and the similar values of **C**_{BiPh} and **C**_{BiPh/Hex}. For **C**_{BiPh}, we note a DQI feature at 0.61 eV. To investigate the origin of the DQI, we have included additional calculations in the ESI[†] (Figure S21 and S22). The DQI feature appears exclusively in the **C**_{BiPh} system and disappears when either the hexane backbone or the biphenyl backbone is removed. This suggests that very subtle effects control the magnitude of the transmission through the system. We hesitate to speculate about the details of what is controlling this effect, and instead just note that this result highlights the limitation of viewing a single quantum system like a molecule as a sum of paths.^[23]

We also explored how the electronic energy of the **A**_{Stilb}-Au nanojunction evolves as the Au tips are being pushed closer and closer together, starting from the *transoid* structure at an initial tip distance of 1.92 nm. Initially, the immobilized **A**_{Stilb} molecule responds to the increasing

mechanical stress by rotation around mainly the N-aryl bonds at the anchor group-modified aryl rings. However, further compression of the junction forces $\mathbf{A}_{\text{Stilb}}$ to rotate around the N-linker bonds, thereby converting *transoid* into *cisoid* structures. This change is computed to occur at an electrode displacement of 0.89 nm and guides the system into a new local energy minimum (for details see Figure S18 in the ESI[†]).

Flicker Noise Analysis

In order to investigate and elaborate the differences between the high- and low- G features of $\mathbf{A}_{\text{Stilb}}$ in even more detail, we performed flicker noise analysis. This method probes the relation between the power spectrum density (PSD) and the average conductance (G_{ave}) as $\text{PSD} \propto G_{\text{ave}}^N$ and can provide additional information with respect to the intricacies of the molecule-metal junction.^[8f,10,24] Flicker noise is assumed to arise mainly from fluctuations in the electronic coupling Γ between the probe molecule within the gap and the electrodes. These fluctuations were previously ascribed to a restructuring of the electrodes imposed by positional changes of metal atoms during the experiment.^[24b]

In order to evaluate the average conductance G_{ave} and the power spectrum density PSD, the linear tip displacement was stopped for 250 ms at a position where a stable junction with the molecule in the compressed or the stretched geometry was likely to form. The conductance was then recorded at a bias voltage of 100 mV and at an acquisition rate of 40 kHz.^[24b] We employed a specific selection algorithm to identify relevant segments within our data sets that corresponded to either the high- or the low- G states, thereby allowing us to analyze the flicker noise for both separately.

In our analysis, we only considered traces that contain >4000 data points, which is the minimum value required for reliable PSD analyses, and for which the mean conductance between the first 400 and the last 1000 data points fall within the limits of $\log(G/G_0) = -4.4 \pm 0.56$ for the low- G state, and $\log(G/G_0) = -2.9 \pm 0.26$ for the high- G state. Panel A of Figure 5 displays a representative trace for each state. A Fourier transform was then applied to the segments enclosed within the vertical, dashed lines to obtain the PSD, shown in panel B of Figure 5. We then integrated the noise power between 0.1 and 1 kHz, as indicated by the black, dashed lines in panel B of Figure 5. Integration was performed for all qualifying traces, and the resulting noise powers were normalized by the average conductance within the Fourier-transformed segment of each trace. The normalized noise powers are visualized as 2D histograms in panels C (high- G state) and D (low- G state) of Figure 5. By fitting a 2D Gaussian to each 2D-histogram, we calculated the so-called ‘scaling exponent’ N according to the power law $\text{PSD} \propto G_{\text{ave}}^N$.^[24b] Sensitivity analysis of the scaling exponent according to the procedure detailed in the ESI[†] provided standard deviations as a probe for its variability depending on the evaluation parameters.

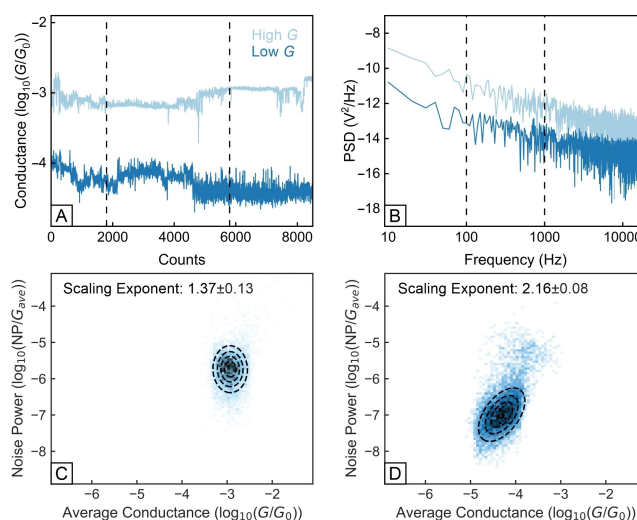


Figure 5. A: Two representative traces of $\mathbf{A}_{\text{Stilb}}$ with an average conductance value between the dashed, black vertical lines of $-4.4 \pm 0.56 \log_{10}(G/G_0)$ (darkblue, low- G trace) and $-2.9 \pm 0.26 \log_{10}(G/G_0)$ (light-blue, high- G trace). B: Power spectrum density obtained by Fourier transformation of the traces displayed in (A). C: 2D Histogram showing the normalized noise power vs. average conductance G_{ave} for the high- G traces of $\mathbf{A}_{\text{Stilb}}$ with the corresponding scaling exponent $N = 1.39 \pm 0.19$. D: 2D Histogram showing the normalized noise power vs. average conductance G_{ave} for the low- G traces of $\mathbf{A}_{\text{Stilb}}$ with the corresponding scaling exponent $N = 2.04 \pm 0.07$.

As mentioned above, the scaling exponent N provides a measure of the strength of electrode/molecule coupling and fluctuations within the junction. A value close to 1 signals that the probe molecule is electronically strongly coupled to the tip, whereas an exponent N of 2 suggests that the junction is fluxional and subject to constant changes in Γ .^[24b]

If the different states have the same binding configuration, N can be used as an indicator of the principal conductance mechanism and to discriminate between through-space and through-bond pathways,^[8f,10,24] but this might not be the case here as we see a phenyl-assisted coupling of the thiomethyl anchor in the *cisoid* conformer (cf. panel A of Figure 3).

Thus, we use the scaling exponent as a measure of coupling strength between molecule and electrodes. For junctions with $\mathbf{A}_{\text{Stilb}}$ in the compressed, *cisoid* conformation representing the high- G state, we obtain a scaling exponent $N = 1.39 \pm 0.19$, indicating strong interactions between the molecule and the electrodes and small fluctuations in Γ . This aligns well with the computed junction geometry shown in panel A of Figure 3, where we see the phenyl-assisted coupling to the electrodes. For junctions in the low- G state, the scaling exponent is 2.04 ± 0.07 , which suggests much stronger fluctuations in Γ . In the present case, fluctuations may arise not only from changes of the atomic positions of the Au atoms, but also from conformational flexibility, i.e., from rotations around the C–N bonds of the TAA subunits. Such rotation is not possible when the molecule is in a compressed state.

In summary, the results from flicker noise analysis are congruent with those of the theoretical modeling. Both indicate strong coupling between the electrode and molecules of **A_{Stilb}** as well as a stable junction configuration for the *cisoid*, high-*G* conformer, and much higher variability and fluxionality for the low-*G* state, where **A_{Stilb}** adopts a stretched structure with *transoid* disposed SME anchor groups.

Conclusions

The acyclic SME-functionalized bis(triarylamines) **A_{Stilb}** and **A_{BiPh}** with a *cis*-stilbenyl or a biphenylene linker between the amine N atoms constitute molecular conductance switches that are triggered by large-amplitude conformational changes between a compressed and a stretched state. Replacing the stilbenyl linker of **A_{Stilb}** by the *meta,meta*-biphenyl linker of **A_{BiPh}** with its inherent destructive quantum interference pattern increases the *on/off* ratio $G_{\text{high}}/G_{\text{low}}$ from 60 to $\sim 10^3$. This renders **A_{BiPh}** one of the best-performing single-molecule conductance switches reported in the literature.^[8b,c,f] Push-pull experiments demonstrate that switching between the two states is reversible over several cycles of stretching and compressing the junction. Comparison of **A_{Stilb}** and **A_{BiPh}** with specifically tailored cyclic counterparts that are constrained to either the stretched or the compressed conformation clearly demonstrates, that the switching properties of **A_{Stilb}** and **A_{BiPh}** depend crucially on the availability of a wide, but well-defined, conformational space.

DFT-based transport calculations reveal that conductance switching in **A_{Stilb}** and **A_{BiPh}** does, however, not simply rely on a large-amplitude change of the spatial separation between the anchor groups, but also involves a change of the transmission pathway, from across the molecular backbone for the stretched conformers to a shortcut over the SME anchor groups that bypasses the π -conjugated backbone. Analysis of the optimized junction geometries further suggested that particularly strong electronic coupling between the molecules and the electrodes in the compressed states contributes to its high conductance. Flicker noise analysis supports this idea and reveals considerable differences between the high- and low-*G* states, where the junction is fluxional. In conclusion, we have presented a prototype of high-performing conductance switches that rely on the simultaneous, congruent toggling between two different conformations and two principle transmission paths.

Supporting Information

The authors have cited additional references within the Supporting Information.^[25]

Authors Contribution

M. N. devised the project together with R. F. W. M. N. conducted all chemical syntheses, spectroscopic characterizations, conductance measurements and performed DFT calculations of isolated molecules. M. N. and W. B.-J. conducted data analysis. W. B.-J. carried out all DFT-based transport calculations and DFT on the molecular junctions, supervised by G. C. S. M. L. and M. B. performed X-ray diffraction experiments and structure refinement. M. N. and W. B.-J. wrote the initial draft. All authors contributed in scientific discussions.

Acknowledgements

This project was partly funded from the European Research Council (ERC) under the European Union's Horizon 2020 research and innovation programme (grant agreement No 865870). M. N. gratefully acknowledges funding by the Fonds der Chemischen Industrie. R. F. W. and M. N. acknowledge support by the state of Baden-Württemberg and the Deutsche Forschungsgemeinschaft through bwHPC and access to the supercomputing facilities of JUSTUS2 (grant number INST 40/575-1 FUGG). This work was supported by the core facilities of the University of Konstanz through NMR spectroscopic and mass spectrometric measurements. M. N. thanks Kai Jellinek for his motivated support in synthesizing two compounds of this work during his internship. This Open-Access publication was supported by the Publication Fund of the University of Konstanz. Open Access funding enabled and organized by Projekt DEAL.

Conflict of Interest

The authors declare no conflict of interest.

Data Availability Statement

The X-Ray crystallographic data can be obtained free of charge from <http://www.ccdc.cam.ac.uk/conts/retrieving.html>.^[12] The experimental STM-BJ data can be accessed via DOI: 10.17894/ucph.e63ad433-a7fe-48a7-9a96-2f1a417c97fa and all optimized junction structures and their input files for the geometry optimization can be obtained from DOI: 10.19061/iochem-bd-9-8.

Keywords: Charge Transport • Conductance Switch • Macrocycles • Molecular electronics

- [1] a) J. C. Cuevas, E. Scheer, *Molecular Electronics: An Introduction to Theory and Experiment* (World Scientific Series in Nanoscience and Nanotechnology), World Scientific, Singapore 2010; b) D. Xiang, X. Wang, C. Jia, T. Lee, X. Guo, *Chem. Rev.* 2016, 116, 4318–4440.

- [2] N. Xin, J. Guan, C. Zhou, X. Chen, C. Gu, Y. Li, M. A. Ratner, A. Nitzan, J. F. Stoddart, X. Guo, *Nat. Rev. Phys.* **2019**, *1*, 211–230.
- [3] M. Kamenetska, J. R. Widawsky, M. Dell'Angela, M. Frei, L. Venkataraman, *J. Chem. Phys.* **2017**, *146*, 092311.
- [4] R. J. Brooke, D. S. Szumski, A. Vezzoli, S. J. Higgins, R. J. Nichols, W. Schwarzacher, *Nano Lett.* **2018**, *18*, 1317–1322.
- [5] a) X. Yin, Y. Zang, L. Zhu, J. Z. Low, Z.-F. Liu, J. Cui, J. B. Neaton, L. Venkataraman, L. M. Campos, *Sci. Adv.* **2017**, *3*, eaao2615; b) L. Li, J. Z. Low, J. Wilhelm, G. Liao, S. Gunasekaran, C. R. Prindle, R. L. Starr, D. Golze, C. Nuckolls, M. L. Steigerwald, F. Evers, L. M. Campos, X. Yin, L. Venkataraman, *Nat. Chem.* **2022**, *14*, 1061–1067.
- [6] Y. Zang, Q. Zou, T. Fu, F. Ng, B. Fowler, J. Yang, H. Li, M. L. Steigerwald, C. Nuckolls, L. Venkataraman, *Nat. Commun.* **2019**, *10*, 4482.
- [7] a) T. Sandler, K. Luka-Guth, M. Wieser, Lokamani, J. Wolf, M. Helm, S. Gemming, J. Kerbusch, E. Scheer, T. Huhn, A. Erbe, *Adv. Sci.* **2015**, *2*, 1500017; b) M. Tan, F. Sun, X. Zhao, Z. Zhao, S. Zhang, X. Xu, A. Adijiang, W. Zhang, H. Wang, C. Wang, Z. Li, E. Scheer, D. Xiang, *J. Am. Chem. Soc.* **2024**, *146*, 6856–6865; c) J. Koo, Y. Jang, L. Martin, D. Kim, H. Jeong, K. Kang, W. Lee, J. Kim, W.-T. Hwang, D. Xiang, E. Scheer, M. Kabdulov, T. Huhn, F. Pauly, T. Lee, *ACS Appl. Mater. Interfaces* **2019**, *11*, 11645–11653; d) Y. Kim, T. J. Hellmuth, D. Sysoiev, F. Pauly, T. Pietsch, J. Wolf, A. Erbe, T. Huhn, U. Groth, U. E. Steiner, E. Scheer, *Nano Lett.* **2012**, *12*, 3736–3742.
- [8] a) M. Camarasa-Gómez, D. Hernangómez-Pérez, M. S. Inken, G. Lovat, E.-D. Fung, X. Roy, L. Venkataraman, F. Evers, *Nano Lett.* **2020**, *20*, 6381–6386; b) P. Zhou, Y. Fu, M. Wang, R. Qiu, Y. Wang, J. F. Stoddart, Y. Wang, H. Chen, *J. Am. Chem. Soc.* **2023**, *145*, 18800–18811; c) L.-Q. Pei, J. R. Horsley, J.-W. Seng, X. Liu, Y. Q. Yeoh, M.-X. Yu, X.-H. Wu, A. D. Abell, J.-F. Zheng, X.-S. Zhou, J. Yu, S. Jin, *ACS Appl. Mater. Interfaces* **2021**, *13*, 57646–57653; d) T. A. Su, H. Li, M. L. Steigerwald, L. Venkataraman, C. Nuckolls, *Nat. Chem.* **2015**, *7*, 215–220; e) I. Franco, C. B. George, G. C. Solomon, G. C. Schatz, M. A. Ratner, *J. Am. Chem. Soc.* **2011**, *133*, 2242–2249; f) C. Wu, D. Bates, S. Sangtarash, N. Ferri, A. Thomas, S. J. Higgins, C. M. Robertson, R. J. Nichols, H. Sadeghi, A. Vezzoli, *Nano Lett.* **2020**, *20*, 7980–7986; g) D. Stefani, K. J. Weiland, M. Skripnik, C. Hsu, M. L. Perrin, M. Mayor, F. Pauly, H. S. J. Van Der Zant, *Nano Lett.* **2018**, *18*, 5981–5988; h) T. Frederiksen, C. Munuera, C. Ocal, M. Brandbyge, M. Paulsson, D. Sanchez-Portal, A. Arnau, *ACS Nano* **2009**, *3*, 2073–2080; i) Z. Li, H. Li, S. Chen, T. Froehlich, C. Yi, C. Schönenberger, M. Calame, S. Decurtins, S.-X. Liu, E. Borguet, *J. Am. Chem. Soc.* **2014**, *136*, 8867–8870; j) S. Y. Quek, M. Kamenetska, M. L. Steigerwald, H. J. Choi, S. G. Louie, M. S. Hybertsen, J. B. Neaton, L. Venkataraman, *Nat. Nanotechnol.* **2009**, *4*, 230–234; k) N. Ferri, N. Algethami, A. Vezzoli, S. Sangtarash, M. McLaughlin, H. Sadeghi, C. J. Lambert, R. J. Nichols, S. J. Higgins, *Angew. Chem. Int. Ed.* **2019**, *58*, 16583–16589; l) R. Frisenda, G. D. Harzmann, J. A. Celis Gil, J. M. Thijssen, M. Mayor, H. S. J. van der Zant, *Nano Lett.* **2016**, *16*, 4733–4737; m) J. Li, P. Shen, S. Zhen, C. Tang, Y. Ye, D. Zhou, W. Hong, Z. Zhao, B. Z. Tang, *Nat. Commun.* **2021**, *12*, 167; n) A. M. Ortuño, P. Reiné, L. Álvarez de Cienfuegos, I. R. Márquez, W. Dednam, E. B. Lombardi, J. J. Palacios, E. Leary, G. Longhi, V. Mujica, A. Millán, M. T. González, L. A. Zotti, D. Miguel, J. M. Cuerva, *Angew. Chem. Int. Ed.* **2023**, *62*, e202218640; o) J. Li, P. Shen, Z. Zhuang, J. Wu, B. Z. Tang, Z. Zhao, *Nat. Commun.* **2023**, *14*, 6250; p) A. Sil, M. Alsaqer, C. E. Spano, A. Larbi, S. J. Higgins, C. M. Robertson, M. Graziano, S. Sangtarash, R. J. Nichols, H. Sadeghi, A. Vezzoli, *Small* **2024**, *20*, 2308865.
- [9] C. Jia, A. Migliore, N. Xin, S. Huang, J. Wang, Q. Yang, S. Wang, H. Chen, D. Wang, B. Feng, Z. Liu, G. Zhang, D.-H. Qu, H. Tian, M. A. Ratner, H. Q. Xu, A. Nitzan, X. Guo, *Science* **2016**, *352*, 1443–1445.
- [10] T. Fu, S. Smith, M. Camarasa-Gómez, X. Yu, J. Xue, C. Nuckolls, F. Evers, L. Venkataraman, S. Wei, *Chem. Sci.* **2019**, *10*, 9998–10002.
- [11] a) A. Mang, N. Rotthowe, K. Beltako, M. Linseis, F. Pauly, R. F. Winter, *Nanoscale* **2023**; b) I. J. Olavarria-Contreras, A. Etcheverry-Berrios, W. Qian, C. Gutiérrez-Cerón, A. Campos-Olguín, E. C. Sañudo, D. Dulić, E. Ruiz, N. Aliaga-Alcalde, M. Soler, H. S. J. Van Der Zant, *Chem. Sci.* **2018**, *9*, 6988–6996.
- [12] Deposition Number(s) <https://www.ccdc.cam.ac.uk/services/structures?id=doi:10.1002/anie.202417796> 2365503 (for AS-tilbTol), 2365504 (for AS-tilb), 2365505 (for S22), 2365506 (for C-tilb/Hex), 2365507 (for CHex), 2365508 (for AS-tilb-Fixed-Cis), 2365509 (for CBiPh/Hex), 2365510 (for C-tilb/Pent), 2365511 (for CBiPh). These data are provided free of charge by the Cambridge Crystallographic Data Centre <http://www.ccdc.cam.ac.uk/structures>.
- [13] a) B. Xu, N. J. Tao, *Science* **2003**, *301*, 1221–1223; b) L. Venkataraman, J. E. Klare, I. W. Tam, C. Nuckolls, M. S. Hybertsen, M. L. Steigerwald, *Nano Lett.* **2006**, *6*, 458–462; c) L. Venkataraman, J. E. Klare, C. Nuckolls, M. S. Hybertsen, M. L. Steigerwald, *Nature* **2006**, *442*, 904–907.
- [14] a) P. Moreno-García, M. Gulcur, D. Z. Manrique, T. Pope, W. Hong, V. Kaliginedi, C. Huang, A. S. Batsanov, M. R. Bryce, C. Lambert, T. Wandlowski, *J. Am. Chem. Soc.* **2013**, *135*, 12228–12240; b) C. Huang, A. V. Rudnev, W. Hong, T. Wandlowski, *Chem. Soc. Rev.* **2015**, *44*, 889–901; c) T. Fu, K. Frommer, C. Nuckolls, L. Venkataraman, *J. Phys. Chem. Lett.* **2021**, *12*, 10802–10807.
- [15] Y. Zhu, Y. Zhou, L. Ren, J. Ye, H. Wang, X. Liu, R. Huang, H. Liu, J. Liu, J. Shi, P. Gao, W. Hong, *Angew. Chem. Int. Ed.* **2023**, *62*, e202302693.
- [16] a) Y. S. Park, A. C. Whalley, M. Kamenetska, M. L. Steigerwald, M. S. Hybertsen, C. Nuckolls, L. Venkataraman, *J. Am. Chem. Soc.* **2007**, *129*, 15768–15769; b) M. H. Garner, H. Li, Y. Chen, T. A. Su, Z. Shangguan, D. W. Paley, T. Liu, F. Ng, H. Li, S. Xiao, C. Nuckolls, L. Venkataraman, G. C. Solomon, *Nature* **2018**, *558*, 415–419.
- [17] a) C. R. Arroyo, S. Tarkuc, R. Frisenda, J. S. Seldenthuis, C. H. M. Woerde, R. Eelkema, F. C. Grozema, H. S. J. van der Zant, *Angew. Chem. Int. Ed.* **2013**, *52*, 3152–3155; b) T. Stuyver, S. Fias, F. d Proft, P. Geerlings, *J. Phys. Chem. C* **2015**, *119*, 26390–26400; c) G. C. Solomon, D. Q. Andrews, T. Hansen, R. H. Goldsmith, M. R. Wasielewski, R. P. Van Duyne, M. A. Ratner, *J. Chem. Phys.* **2008**, *129*; d) T. Hansen, G. C. Solomon, D. Q. Andrews, M. A. Ratner, *J. Chem. Phys.* **2009**, *131*, 194704; e) A. Borges, J. Xia, S. H. Liu, L. Venkataraman, G. C. Solomon, *Nano Lett.* **2017**, *17*, 4436–4442; f) S.-H. Ke, W. Yang, H. U. Baranger, *Nano Lett.* **2008**, *8*, 3257–3261; g) T. Markussen, R. Stadler, K. S. Thygesen, *Nano Lett.* **2010**, *10*, 4260–4265; h) X. Zhao, V. Geskin, R. Stadler, *J. Chem. Phys.* **2017**, *146*, 092308.
- [18] Y. S. Park, J. R. Widawsky, M. Kamenetska, M. L. Steigerwald, M. S. Hybertsen, C. Nuckolls, L. Venkataraman, *J. Am. Chem. Soc.* **2009**, *131*, 10820–10821.
- [19] a) H. Vazquez, R. Skouta, S. Schneebeli, M. Kamenetska, R. Breslow, L. Venkataraman, M. S. Hybertsen, *Nat. Nanotechnol.* **2012**, *7*, 663–667; b) M. Magoga, C. Joachim, *Phys. Rev. B* **1999**, *59*, 16011–16021.
- [20] A. K. Ismael, K. Wang, A. Vezzoli, M. K. Al-Khaykanee, H. E. Gallagher, I. M. Grace, C. J. Lambert, B. Xu, R. J. Nichols, S. J. Higgins, *Angew. Chem. Int. Ed.* **2017**, *56*, 15378–15382.

- [21] a) A. Jensen, M. H. Garner, G. C. Solomon, *J. Phys. Chem. C* **2019**, 123, 12042–12051; b) W. Bro-Jørgensen, G. C. Solomon, *J. Phys. Chem. A* **2023**, 127, 9003–9012.
- [22] a) F. Evers, F. Weigend, M. Koentopp, *Phys. Rev. B* **2004**, 69, 235411; b) S. Y. Quek, L. Venkataraman, H. J. Choi, S. G. Louie, M. S. Hybertsen, J. B. Neaton, *Nano Lett.* **2007**, 7, 3477–3482; c) D. J. Mowbray, G. Jones, K. S. Thygesen, *J. Chem. Phys.* **2008**, 128; d) T. Markussen, C. Jin, K. S. Thygesen, *Phys. Status Solidi B* **2013**, 250, 2394–2402.
- [23] G. C. Solomon, D. Q. Andrews, R. P. Van Duyne, M. A. Ratner, *ChemPhysChem* **2009**, 10, 257–264.
- [24] a) A. Magyarkuti, O. Adak, A. Halbritter, L. Venkataraman, *Nanoscale* **2018**, 10, 3362–3368; b) O. Adak, E. Rosenthal, J. Meisner, E. F. Andrade, A. N. Pasupathy, C. Nuckolls, M. S. Hybertsen, L. Venkataraman, *Nano Lett.* **2015**, 15, 4143–4149.
- [25] a) M. Schmid, *Programming in Igor Pro: A comprehensive introduction*, Middletown, DE **2018**; b) M. J. Frisch, G. W. Trucks, H. B. Schlegel, G. E. Scuseria, M. A. Robb, J. R. Cheeseman, G. Scalmani, V. Barone, G. A. Petersson, H. Nakatsuji, X. Li, M. Caricato, A. V. Marenich, J. Bloino, B. G. Janesko, R. Gomperts, B. Mennucci, H. P. Hratchian, J. V. Ortiz, A. F. Izmaylov, J. L. Sonnenberg, Williams, F. Ding, F. Lipparini, F. Egidi, J. Goings, B. Peng, A. Petrone, T. Henderson, D. Ranasinghe, V. G. Zakrzewski, J. Gao, N. Rega, G. Zheng, W. Liang, M. Hada, M. Ehara, K. Toyota, R. Fukuda, J. Hasegawa, M. Ishida, T. Nakajima, Y. Honda, O. Kitao, H. Nakai, T. Vreven, K. Throssell, J. A. Montgomery Jr., J. E. Peralta, F. Ogliaro, M. J. Bearpark, J. J. Heyd, E. N. Brothers, K. N. Kudin, V. N. Staroverov, T. A. Keith, R. Kobayashi, J. Normand, K. Raghavachari, A. P. Rendell, J. C. Burant, S. S. Iyengar, J. Tomasi, M. Cossi, J. M. Millam, M. Klene, C. Adamo, R. Cammi, J. W. Ochterski, R. L. Martin, K. Morokuma, O. Farkas, J. B. Foresman, D. J. Fox, Wallingford, CA, USA **2016**; c) M. Cossi, N. Rega, G. Scalmani, V. Barone, *J. Comput. Chem.* **2003**, 24, 669–681; d) S. Grimme, J. Antony, S. Ehrlich, H. Krieg, *J. Chem. Phys.* **2010**, 132; e) S. Grimme, S. Ehrlich, L. Goerigk, *J. Comput. Chem.* **2011**, 32, 1456–1465; f) D. G. A. Smith, L. A. Burns, K. Patkowski, C. D. Sherrill, *J. Phys. Chem. Lett.* **2016**, 7, 2197–2203; g) P. C. Hariharan, J. A. Pople, *Theor. Chim. Acta* **1973**, 28, 213–222; h) J. P. Perdew, K. Burke, M. Ernzerhof, *Phys. Rev. Lett.* **1996**, 77, 3865–3868; i) C. Adamo, V. Barone, *J. Chem. Phys.* **1999**, 110, 6158–6170; j) F. Weigend, R. Ahlrichs, *Phys. Chem. Chem. Phys.* **2005**, 7, 3297; k) F. Weigend, *Phys. Chem. Chem. Phys.* **2006**, 8, 1057–1065; l) Y. Zhao, N. E. Schultz, D. G. Truhlar, *J. Chem. Theory Comput.* **2006**, 2, 364–382; m) V. Barone, M. Cossi, *J. Phys. Chem. A* **1998**, 102, 1995–2001; n) M. S. José, A. Emilio, D. G. Julian, G. Alberto, J. Javier, O. Pablo, S.-P. Daniel, *J. Phys. Condens. Matter* **2002**, 14, 2745; o) M. Brandbyge, J.-L. Mozos, P. Ordejón, J. Taylor, K. Stokbro, *Phys. Rev. B* **2002**, 65, 165401; p) M. Casey, J. Leonard, B. Lygo, G. Procter, in *Advanced practical organic chemistry* (Eds.: M. Casey, J. Leonard, B. Lygo), Blackie, Glasgow **1990**, pp. 28–42; q) O. V. Dolomanov, L. J. Bourhis, R. J. Gildea, J. A. K. Howard, H. Puschmann, *J. Appl. Crystallogr.* **2009**, 42, 339–341; r) G. M. Sheldrick, *Acta Crystallogr. Sect. A* **2015**, 71, 3–8; s) G. M. Sheldrick, *Acta Crystallogr. Sect. C* **2015**, 71, 3–8; t) A. L. Spek, *J. Appl. Crystallogr.* **2003**, 36, 7–13; u) Y. Zhao, C. Ye, Y. Qiao, W. Xu, Y. Song, D. Zhu, *Tetrahedron* **2012**, 68, 1547–1551; v) Y. Song, C. Di, X. Yang, S. Li, W. Xu, Y. Liu, L. Yang, Z. Shuai, D. Zhang, D. Zhu, *J. Am. Chem. Soc.* **2006**, 128, 15940–15941; w) J. Zhu, W. Song, T. Zhang, Q. Dong, J. Huang, H. Zhou, J. Su, *Dyes Pigm.* **2021**, 186, 108981; x) Stoe & Cie **2002**; y) Rigaku Oxford Diffraction Ltd **2024**; z) L. J. Bourhis, O. V. Dolomanov, R. J. Gildea, J. A. K. Howard, H. Puschmann, *Acta Crystallogr. Sect. A* **2015**, 71, 59–75; aa) F. Kleemiss, O. V. Dolomanov, M. Bodensteiner, N. Peyerimhoff, L. Midgley, L. J. Bourhis, A. Genoni, L. A. Malaspina, D. Jayatilaka, J. L. Spencer, F. White, B. Grundkötter-Stock, S. Steinhauer, D. Lentz, H. Puschmann, S. Grabowsky, *Chem. Sci.* **2021**, 12, 1675–1692; ab) A. Borges, E. D. Fung, F. Ng, L. Venkataraman, G. C. Solomon, *J. Phys. Chem. Lett.* **2016**, 7, 4825–4829.

Manuscript received: September 16, 2024

Version of record online: December 4, 2024